ELSEVIER

Journal of Nuclear Materials 297 (2001) 161–175

journal of nuclear materials

www.elsevier.com/locate/jnucmat

Microstructure evolution in austenitic Fe–Cr–Ni alloys irradiated with rotons: comparison with neutron-irradiated microstructures

J. Gan [a,*], G.S. Was [b]

[a] *Pacific Northwest National Laboratory, Material Interface Group, MSIN P8-16, P.O. Box 999, Richland, WA 99352, USA*
[b] *Nuclear Engineering and Radiological Sciences and Materials Science and Engineering, University of Michigan, Ann Arbor, MI, USA*

Received 24 July 2000; accepted 2 May 2001

Abstract

Irradiation-induced microstructures of high purity and commercial purity austenitic stainless steels were investigated using proton-irradiation. For high purity alloys, Fe–20Cr–9Ni (HP 304 SS), Fe–20Cr–24Ni and Ni–18Cr–9Fe were irradiated using 3.2 MeV protons between 300°C and 600°C at a dose rate of 7×10^{-6} dpa/s to doses up to 3.0 dpa. The commercial purity alloys, CP 304 SS and CP 316 SS were irradiated at 360°C to doses between 0.3 and 5.0 dpa. The dose, temperature and composition dependence of the number density and size of dislocation loops and voids were characterized. The changes in yield strength due to irradiation were estimated from Vickers hardness measurements and compared to calculations using a dispersed-barrier-hardening (DBH) model. The dose and temperature dependence of proton-irradiated microstructure (loops, voids) and the irradiation hardening are consistent with the neutron-data trend. Results indicate that proton-irradiation can accurately reproduce the microstructure of austenitic alloys irradiated in LWR cores. © 2001 Published by Elsevier Science B.V.

1. Introduction

Material degradation due to irradiation damage in nuclear reactor core components has been investigated for more than four decades. It is a continuing effort to understand how the degradation occurs under irradiation in order to provide guidance in the development of new, more resistant alloys and to optimize the performance of existing alloys. Structural materials in light water reactor (LWR) cores are predominantly made from austenitic stainless steels (SS), which while in service, are in contact with high temperature water (typically 270–340°C) and exposed to neutron-irradiation. Irradiation-induced microstructure and microchemistry changes are believed to be the key variables responsible for component failures in light water reactor cores.

Although several reviews have been written about irradiation effects on microstructure in stainless steels [1–3], the evolution of microstructure under irradiation conditions relevant to LWR cores is still not fully understood partially due to the lack of data. This lack of data are in part due to the fact that material degradation in light water reactor was underestimated. Once the problem of material degradation in LWR core was realized, the cost of irradiation and testing became an issue due to the need for lengthy irradiations, the difficulty in controlling the irradiation conditions, and the cost of handling neutron-irradiated materials. Months to years of irradiation time are required to obtain modest doses (a few dpa) at displacement rates characteristic of LWR core structural materials ($\sim 10^{-8}$ dpa/s). Due to the high radioactivity, samples removed from the reactor need to undergo a cooling period during which the activities of the short-lived isotopes decay to a safe level before they can be subjected to microstructure analysis. Special procedures and facilities are needed to prepare neutron-irradiated samples for microstructure analysis using transmission electron microscopy (TEM).

* Corresponding author. Tel.: +1-509 376 6372; fax: +1-509 376 6308.
E-mail address: jian.gan@pnl.gov (J. Gan).

0022-3115/01/$ - see front matter © 2001 Published by Elsevier Science B.V.
PII: S0022-3115(01)00615-8

The objective of this work is to understand the microstructure evolution under irradiation conditions relevant to LWR core internal components. High energy proton-irradiation of stainless steels ($\sim 7 \times 10^{-6}$ dpa/s) can produce irradiation doses of a few dpa in days, compared to years in reactor ($\sim 10^{-8}$ dpa/s). Protons have the same mass as neutrons and are capable of producing an approximately uniform damage layer of several tens of microns ($\sim$35 μm for 3.2 MeV protons) [4]. Although difference existed between proton and neutron-irradiation, e.g., cascade morphology, transmutation product, etc., proton-irradiation has shown to be effective in producing similar irradiated microstructure as that of neutron-irradiation [5]. The advantage of using proton irradiation is in the control over irradiation conditions (dose rate and temperature) and low residual radioactivity, allowing microstructure analysis to be done more quickly and less costly than in the case of neutron-irradiation. This quick turn-around time makes it possible to look at the effects of dose, temperature and composition on the irradiated microstructure over many different alloys and irradiation conditions. By establishing the correlation between proton- and neutron-irradiated microstructures of the same alloy and heat, results from proton-irradiation can be used to provide valuable information on microstructure evolution in austenitic stainless steels in LWR cores.

This work is focused on investigating the microstructure of austenitic stainless steels irradiated with protons under conditions relevant to LWR cores. The dislocation loop density and size, the void density and size, and irradiation hardening are determined as functions of dose, temperature and composition, and are compared to those for neutron irradiations of the same or similar alloys. All the irradiation in this work was conducted with 3.2 MeV protons. To establish the correlation between proton- and neutron-irradiated microstructure, high purity (HP) alloys Fe–20Cr–24Ni, Fe–20Cr–9Ni (HP 304 SS), Ni–18Cr–9Fe and commercial purity (CP) alloys, CP 304 SS and CP 316 SS, were irradiated over a broad range of irradiation conditions. The same heats of commercial 304 SS and 316 SS were also irradiated with neutrons in a boiling water reactor (BWR), providing a direct comparison of irradiated microstructure between protons and neutrons without introducing differences in alloy composition and fabrication processes. By analyzing the proton-irradiated microstructure and the available neutron data, the mechanisms of microstructural evolution in austenitic stainless steels under irradiation conditions relevant to LWR core components can be evaluated.

2. Experiment

Alloys were chosen to characterize the irradiated microstructure as a function of dose, temperature and composition in order to examine: (1) the dose dependence and temperature dependence of the irradiated microstructure in high purity alloys, (2) the effect of composition on the irradiated microstructure, and (3) the correlation between irradiation-induced microstructure and hardening of neutron- and proton-irradiated alloys (same heats of commercial grade 304 SS and 316 SS). The chemical compositions for all the alloys used in this study are listed in Table 1. The summary of irradiation temperature and dose conditions for each alloy used in this work is listed in Table 2. Fe–20Cr–24Ni was used to determine the dose dependence between 0 and 3.0 dpa at 400°C, and temperature dependence over the range 300–600°C at a dose of 0.5 dpa. Alloys, Fe–20Cr–9Ni, Fe–20Cr–24Ni and Ni–18Cr–9Fe, were used to investigate the effect of solute composition on the irradiated microstructure at an irradiation temperature of 400°C. All the high purity alloys investigated were supplied by the General Electric Company. Alloys, CP 304 SS and 316 SS, received from ABB in Sweden, were used for the direct comparison of irradiated micro-

Table 1
Chemical composition of the alloys used in this work (at.%)[a]

Alloy element	Fe–20Cr–9Ni	Fe–20Cr–24Ni	Ni–18Cr–9Fe	CP 304	CP 316
Cr	20.72	20.0	18.26	19.3	17.83
Ni	8.88	23.2	72.36	7.94	11.54
Fe	69.16	55.5	9.32	69.37	65.66
Mn	1.11	1.15	0.010	1.38	1.77
Mo	<0.01	0.06	0.002	0.21	1.49
Si	0.09	<0.01	0.027	1.27	1.17
C	0.021	0.012	0.014	0.16	0.18
N	<0.004	0.008	NM	0.266	0.23
P	0.01	<0.01	0.007	0.055	0.043
S	<0.01	<0.009	0.004	0.05	0.012
O	0.029	0.055	NM	NM	NM
B	NM	NM	NM	<0.002	0.067

[a] NM: Not measured.

Table 2
Summary of irradiation temperature and dose conditions for each alloy used in this work

Alloy	Temperature (°C)	Dose (dpa)
Dose dependence		
Fe–20Cr–9Ni	400	0.1
	400	0.5
	400	1.0
	400	3.0
Fe–20Cr–24Ni	400	0.5
	400	1.0
	400	3.0
Ni–18Cr–9Fe	400	0.1
	400	0.3
	400	0.5
	400	1.0
CP 304 SS	360	0.5
	360	1.0
	360	3.0
	360	5.0
CP 316 SS	360	1.0
	360	3.0
	360	5.0
Temperature dependence		
Fe–20Cr–9Ni	335	1.0
	360	1.0
	400	1.0
Fe–20Cr–24Ni	300	0.5
	400	0.5
	500	0.5
	600	0.5

structure and yield strength changes with the same heats irradiated in a BWR. The initial properties of the materials used in this study are listed in Table 3, where the estimated values of shear modulus (76 GPa, [6]) and lattice constant (3.55 Å, [7]) for austenitic stainless steel were used for all the alloys.

The high purity alloys, in the form of 12 mm thick bars, were solution-annealed at 1100°C for 1 h to produce a homogeneous microstructure and microchemistry and a grain size of 100–200 μm. The alloys were then cold-rolled from 12 mm down to 4 mm to provide a reduced grain size upon recrystallization. The material was mechanically cut into bar samples with dimensions of $1.5 \times 4.0 \times 30$ mm^3, and then wet-polished using 320–600 grit waterproof silicon carbide (SiC) paper to remove the mechanical damage induced during machining. The final annealing treatment in a flowing argon atmosphere at 850°C for 30 min recrystallized the alloys to achieve grain sizes of approximately 10 μm. These bar samples were further wet-polished using 1200–2400 grit SiC paper to obtain a mirror-like surface. For the commercial purity alloys (CP 304 and CP 316), the as-received alloys were cut into bar samples using electric discharge machining (EDM) to minimize the mechanically damaged layer. No heat treatment was given to these samples. After wet-polishing, all the samples were electro-polished in a solution of 60% phosphoric acid and 40% sulfuric acid for 3 min at approximately 42°C to provide a smooth surface prior to irradiation.

Irradiations were performed using a tandem accelerator (the General Ionex Tandetron) at the Michigan Ion Beam Laboratory for Surface Modification and Analysis at the University of Michigan [8]. All irradiations were conducted using 3.2 MeV protons in a vacuum better than 3×10^{-8} Torr. Protons with this energy produce a nearly uniform damage layer in the first 35 μm of the proton range (40 μm) as calculated using a program package of the range of ions in matter (TRIM) [9]. The irradiation dose and temperatures ranged from 0.1 to 5.0 dpa and 300–600°C, respectively. The details of the irradiations can be found in a previous work [4]. The dose uniformity of the irradiated samples was checked using a Tennelec LB 5100 automated α/β counter by measuring the activity in units of β–counts/min/mm^2 within the same irradiation batch.

Irradiated bar samples were back-thinned to a thickness of ~300 μm from the unirradiated side using wet-polishing (180–320 grit SiC paper). TEM disks were cut using a slurry drill core-cutter to minimize mechanical damage. TEM disks were further wet-polished from the unirradiated side down to a thickness of 100–140 μm using 400–2400 grit SiC paper. A solution of 5% perchoric acid (in 75% concentration) in methanol was used for jet electrochemical polishing. A single-jet unit

Table 3
Initial properties of the materials used in this work

	Grain size d_{grain} (μm)	Vickers hardness H_v (kg/mm^2)	Yield strength σ_y (MPa)	Shear modulus[a] μ (GPa)	Lattice constant[b] a_0 (10^{-8} cm)
Fe–20Cr–9Ni	10	176	150	76	3.55
Fe–20Cr–24Ni	11	136	150	76	3.55
Ni–18Cr–9Fe	10	NM[c]	NM[c]	76	3.55
CP 304	60	200	243	76	3.55
CP 316	80	190	228	76	3.55

[a] Estimated from [6].
[b] Estimated from [7].
[c] NM: Not measured.

was used with the solution temperature and polishing current to be −64°C and ~16 mA, respectively. A layer of 5–10 μm was removed from the irradiated side by a 30 s jet-polishing. The sample was then jet-polished from the unirradiated side to obtain a perforation surrounded by thin region. Further thinning with ion milling was often used when jet-polishing failed to produce thin region on the specimen. It was found out that ion milling could create black-dots on the sample, this is partly the reason that black-dot defects were not characterized in this work. The impact of the exclusion of black-dot defects on irradiation hardening will be addressed later in the discussion.

Microstructure analysis was carried out using transmission electron microscopy with a JEOL® 2000FX TEM/STEM. Bright field (BF) imaging, dark field (DF) imaging and rel-rod dark field (RRDF) imaging techniques were used to characterize the microstructure before and after proton-irradiation. Details of the statistical analysis for loop density can be found in the reference [10] The number density and size of dislocation loops and voids were measured from digitized TEM photos using an image-processing program. To ensure a valid comparison of the same heat between proton-irradiated microstructure analyzed at The University of Michigan (UM) and neutron-irradiated microstructures analyzed at Pacific Northwest National Laboratory (PNNL), proton-irradiated sample (CP 316 SS, 3.0 dpa) was analyzed at both UM and PNNL and compared with neutron-irradiated sample (CP 316 SS, 2.9 dpa) for loop size and density. The result of the benchmark for neutron- and proton-irradiated CP 316 SS (~3 dpa) is shown in Fig. 1. There is a discrepancy in loop density that was caused by the resolution problem with the JEOL 2000 electron microscope at UM. As a consequence, the loop measurements for proton-irradiations are adjusted by a factor of 2 to account for the difference in imaging technique.

To evaluate radiation-induced hardening, yield strength changes were estimated from Vickers hardness measurements before and after irradiation. At least 30 measurements were made using a 25 g load at room temperature. According to Higgy and Hammad [11], the yield strength changes due to irradiation for 304 SS can be estimated from hardness changes using the relation

$$\Delta\sigma_y = \frac{\Delta H_V}{2.82}. \tag{1}$$

This gives $\Delta\sigma_y = 3.55\Delta H_V$ where ΔH_V is in kg/mm^2 and $\Delta\sigma_y$ is in MPa. If the unirradiated yield strength (σ_0) is known, the yield strength for the irradiated material can be calculated ($\sigma_y = \sigma_0 + \Delta\sigma_y$).

Radiation-induced hardening was also determined from microstructure measurements by calculating the yield strength change using the dispersed-barrier-hardening (DBH) model [3]. Due to the concern that black-dot defects could also arise from ion milling as mentioned earlier, only the contribution of Frank loops and voids to the irradiation hardening was considered. Irradiation-induced yield strength changes are calculated using Eqs. (2) and (3) for proton-irradiated microstructure ($T = 300$–600°C):

$$\Delta\sigma_y = M\alpha\mu b\sqrt{Nd} \tag{2}$$

and

$$\Delta\sigma_y^{tot} = \sqrt{\left(\Delta\sigma_y^{Loop}\right)^2 + \left(\Delta\sigma_y^{Void}\right)^2}, \tag{3}$$

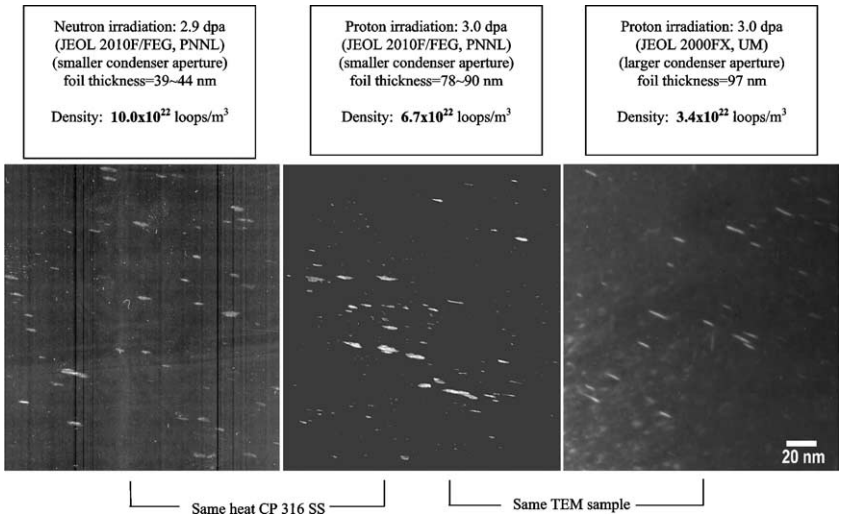

Fig. 1. Photomicrographs of rel-rod dark field images of Frank loops in proton- and neutron-irradiated CP 316 SS for benchmarking of microstructure measurements between UM and PNNL.

where M is Tailor factor ($M = 3.06$, [12]) which relates the shear stresses on a slip plane in a single crystal to the applied tensile stress necessary to activate slip in a polycrystal, α is the barrier strength factor (1.0 for voids, 0.4 for faulted loops [3]), μ is the shear modulus, b is the Burgers vector for network dislocation, N is the defect number density, and d is the mean size of the defects. For austenitic stainless steels, $\mu \approx 76$ GPa [6] and $b = 2.5 \times 10^{-8}$ cm [7] were used for calculation.

3. Results and discussion

The results for the proton-irradiated microstructure and irradiation-induced hardening as functions of irradiation dose and temperature are presented in comparison with neutron-irradiated microstructures. Dislocation loop characterization is presented first, followed by voids and irradiation hardening. Each section describes the effect of dose, temperature and alloy composition with a comparison between proton-irradiation and neutron-irradiation.

3.1. Dislocation loops

3.1.1. Dose dependence

TEM microscopy examination indicated that dislocation loops were the dominant irradiation-induced defects for nearly all the proton irradiation conditions except the irradiation at 600°C for high purity Fe–20Cr–24Ni, in which no dislocation loops were formed. Figs. 2(a) and (b) show the bright field images of dislocation loops as a function of dose (400°C) and temperature (0.5 dpa) in the high purity alloys, Fe–20Cr–24Ni, respectively. The rel-rod dark field images of Frank loops in CP 304 SS and CP 316 SS are shown in Fig. 2(c) and (d). Loop size distributions of proton- and neutron-irradiated commercial purity alloys, CP 304 SS and CP 316 SS, are shown in Fig. 3. At comparable doses, loop size distributions between neutron-irradiation at 275°C and proton irradiation at 360°C are in good agreement. It appears that loop structure developed under neutron-irradiation (275°C, 7×10^{-8} dpa/s) and proton irradiation (360°C, 7×10^{-6} dpa/s) is very similar although there is difference in displacement morphology between neutron and proton-irradiation.

Loop densities resulting from proton-irradiations are plotted with those from neutron-irradiation as a function of dose [2,13–16] in Fig. 4. The alloys used for neutron-irradiation at 275°C and for proton-irradiation at 360°C are from the same heat, providing direct comparison of microstructure evolution between neutron and proton-irradiation. Loop densities in proton-irradiated CP 304 SS and CP 316 SS follow the same trend as for neutron-irradiation at 275°C. This indicates that the partitioning of point defects to loops and other sinks, the balance between nucleation and loss of loops by loop unfaulting and interstitial cluster diffusion, and the evolution of overall sink strength would be similar for neutron and proton-irradiation. While the trends of loop density as a function of dose between neutron and proton-irradiations are in good agreement, there is a tendency that loop density in proton-irradiated CP 304 SS at 360°C is slightly lower than that for neutron-irradiation at 275°C. It appears that the difference in loop densities between neutron and proton irradiation diminishes with increasing of dose. One of the possible reasons for the larger difference at low dose may be the greater difficulty in imaging small loops at low doses where the size is small due to resolution problem with the electron microscope at UM.

The dose dependence of loop density in proton-irradiated (400°C) high purity alloys shows a similar trend to that for neutron irradiation. However, the magnitude of the loop density was lower than that of the proton-irradiated CP material. The lower loop density in proton-irradiated high purity alloys is likely due to the effect of composition on loop nucleation. The higher phosphorus content in commercial alloys ($P = 0.043$–0.055 at.%) than that in high purity alloys ($P \leqslant 0.01$ at.%) enhances interstitial cluster formation through strong binding to interstitials [17], promoting loop nucleation. The higher silicon content in commercial alloys (Si = 1.17–1.27 at.%) than that in high purity alloys (Si $\leqslant 0.09$ at.%) may be also responsible for the higher loop density in CP 304 and CP 316 SS than that in high purity alloys. Silicon is known to enhance the vacancy diffusivity [18]. An increase in vacancy diffusivity may lead to an increase in vacancy loss to sinks, thus the partitioning of interstitials to loops may increase.

The dose dependence of loop size in proton-irradiated CP 304 SS, CP 316 SS, and high purity alloys is shown in Fig. 5, which includes neutron data (275°C, 300°C and 390°C) [13–15]. The data for proton- and neutron-irradiated CP 304 SS and CP 316 SS taken from the same heat are in good agreement. Loop size rapidly increases with dose up to 1 dpa, approaching saturation between 3 and 5 dpa. While loop densities in neutron-irradiated alloys appear to saturate around 3 dpa, the dose for saturation of loop size is less clear, but appears to be between 4 and 5 dpa. Loop size in proton-irradiated high purity Fe–20Cr–24Ni appears to saturate very quickly. The earlier saturation of loop size for proton-irradiated Fe–20Cr–24Ni at 400°C may be caused by a higher void density in this alloy which may alter the partitioning of interstitials to loop.

Proton-irradiation can achieve damage rates several orders of magnitude higher than that of neutron-irradiation in LWR core components. To maintain an equal fraction of defect loss to recombination as for neutron-irradiation, and to have the same defect partitioning to the microstructure, an elevated temperature is required.

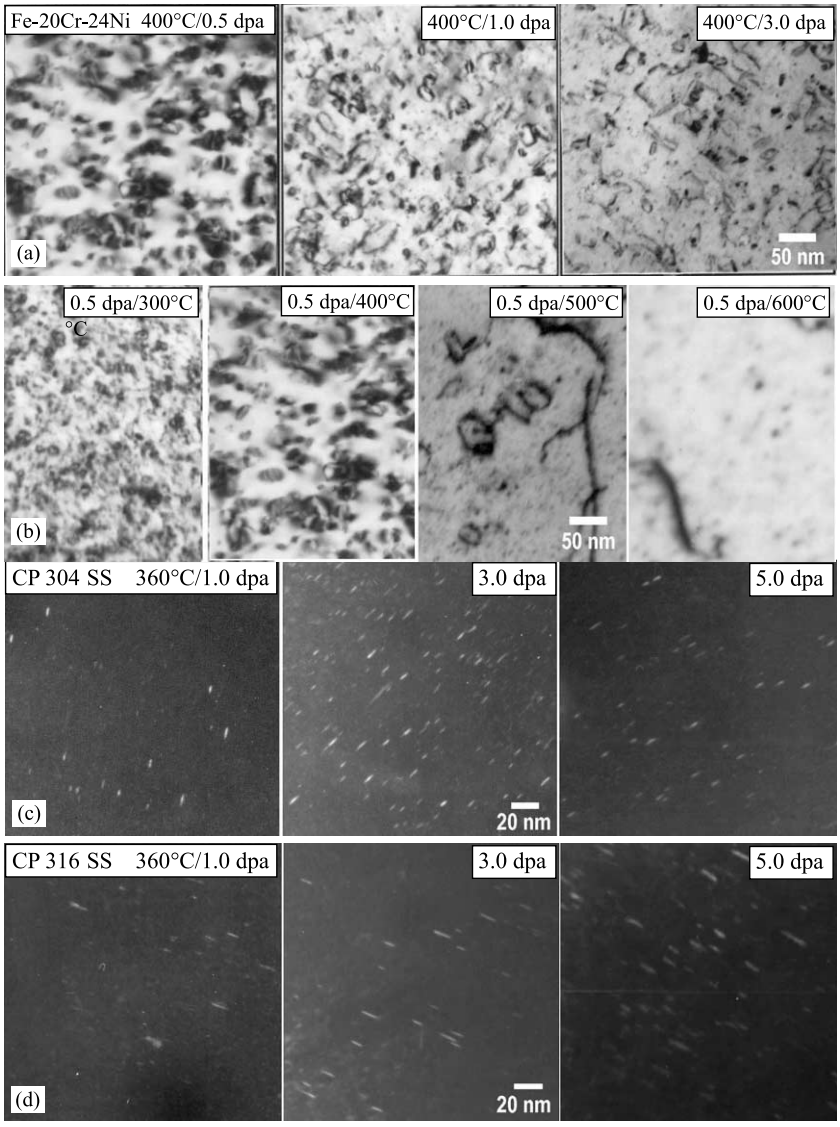

Fig. 2. Photomicrographs showing dislocation loops in bright field images as: (a) a function of dose at irradiation temperature of 400°C and (b) a function of temperature at a dose of 0.5 dpa for proton-irradiated high purity alloys Fe–20Cr–24Ni, and dark field (relrod) for (c) CP 304 SS and (d) CP 316 SS irradiated with protons to 1.0, 3.0 and 5.0 dpa at 360°C.

However, the elevated temperature could affect the microstructure development, especially the overall sink strength. For example, the annihilation of network dislocations is promoted and the loop loss by small interstitial cluster diffusion to sinks is also increased by the upward temperature shift.

The microstructures resulting from neutron and proton-irradiation can still be very similar if the effects of higher dose rate, higher temperature and smaller cascades for proton-irradiation on the defect partitioning and sink development are balanced. Results show that the magnitude of faulted loop density and size at saturation from proton irradiation can be controlled to be very close, if not the same, to that of neutron-irradiation by adjusting the proton-irradiation temperature at a given dose rate.

3.2. Temperature dependence

Photomicrographs of dislocation loops as a function of temperature for high purity Fe–20Cr–24Ni (300–600°C, 0.5 dpa) are shown in Fig. 2(b). The temperature dependence of loop density for both neutron- and proton-irradiated austenitic stainless steels is shown in Fig. 6. Loop densities of proton-irradiated high purity alloy Fe–20Cr–24Ni (300–500°C) and UHP 304 SS

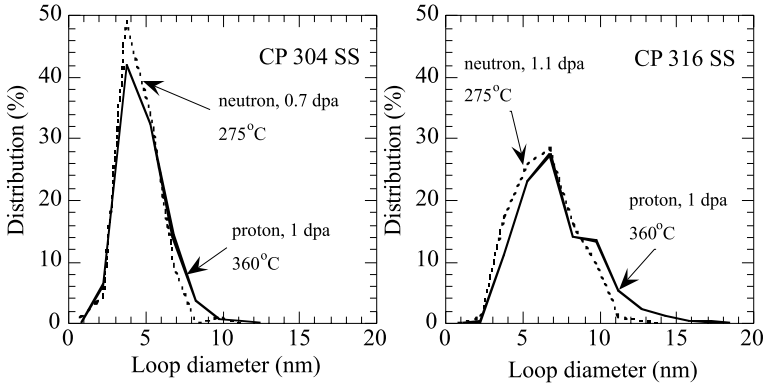

Fig. 3. Comparison of loop size distribution between neutron-irradiated (275°C) and proton-irradiated (360°C) CP 304 SS and CP 316 SS, neutron data were taken from [13].

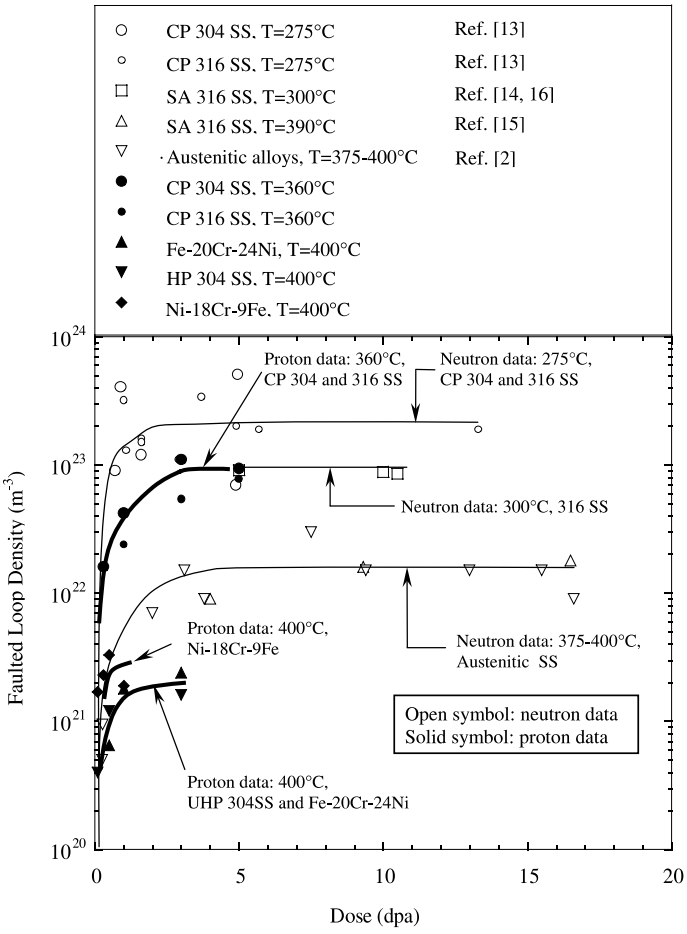

Fig. 4. Dose dependence of faulted loop density between neutron-irradiated (open symbols, 275–400°C) [2,13–16] austenitic stainless steels and proton-irradiated (solid symbols) high purity alloys and commercial purity alloys.

(335–400°C) at doses of 0.5–1.0 dpa are plotted together with neutron data at doses >10 dpa. The temperature dependences for both neutron and proton-irradiation are the same, despite the difference in doses. The lower values of loop density in proton irradiated cases are partly due to the lower doses. While similar results do

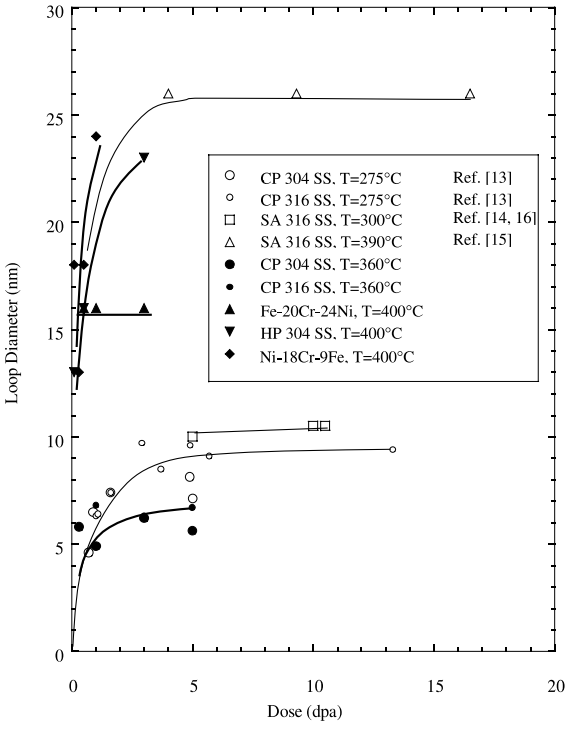

Fig. 5. Dose dependence of loop size between neutron-irradiated (open symbol) [2,13–15] and proton-irradiated (close symbol) austenitic stainless steels.

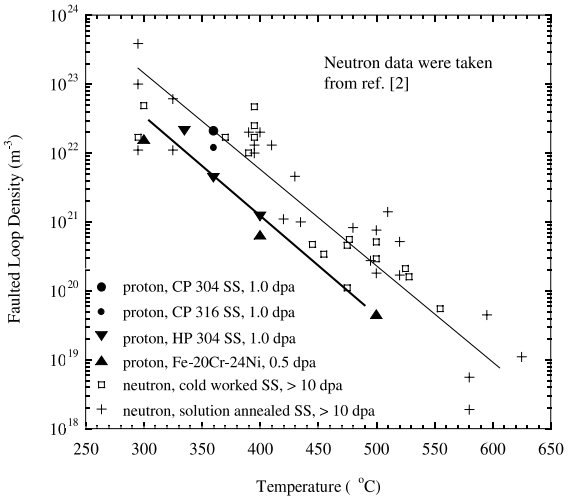

Fig. 6. Temperature dependence of Frank loop density for neutron-irradiated austenitic stainless steels at doses greater than 10 dpa [2] and proton-irradiated high purity and commercial purity alloys at doses of 0.5 and 1.0 dpa.

not insure the process the same, they are consistent with common mechanism.

Loop diameter as a function of temperature for both neutron-irradiated 316 SS [2,15] and proton-irradiated high purity Fe–20Cr–24Ni and UHP 304 SS is shown in Fig. 7. The trends between neutron and proton irradiations are similar. The lower loop diameters in proton-irradiation are due to the lower doses (0.5–1.0 dpa) compared to those for neutron irradiation (5–15 dpa). At temperatures of 400–550°C, the rate of increase in size with temperature is similar for both neutron and proton-irradiation. Loop size seems less sensitive to temperatures between 300°C and 400°C for proton-irradiated high purity alloys, slightly different than that for neutrons. The relatively slow change in loop size with temperature between 300°C and 400°C may reflect a reduction in the partitioning of interstitials to faulted loops caused by an increase in interstitial loss to sinks which are thermally stable (such as vacancy clusters) in the temperature range 300–400°C. There is no noticeable difference between the two high purity alloys. The proton-irradiated CP 304 SS has slightly smaller loop size than does the HP alloy, consistent with the expected effect of impurities on loop characteristics.

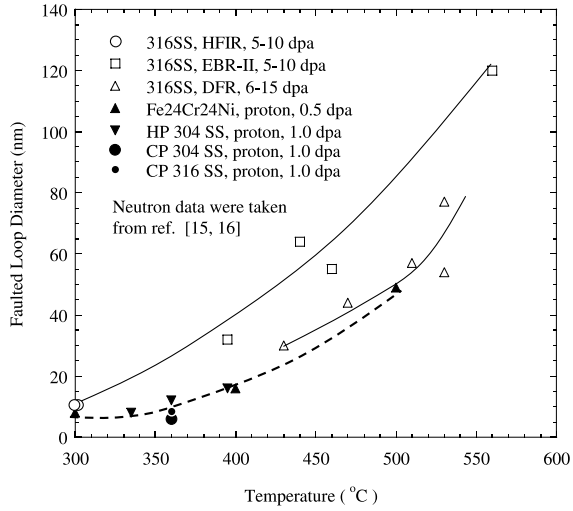

Fig. 7. Temperature dependence of Frank loop size for 316 SS irradiated with neutrons to doses of 5–16 dpa [2,15], together with proton-irradiated alloys.

3.3. Voids

3.3.1. Dose dependence

Photomicrographs of voids as a function of dose for high purity alloy Fe–20Cr–24Ni are shown in Fig. 8(a). Dose dependence of void density for the high purity alloy irradiated with protons at 400°C is shown along with neutron data from 316 SS irradiated at 390°C and 460°C in Fig. 9. Neutron data at lower dose (<20 dpa) and temperature (<500°C) are extremely scarce. The

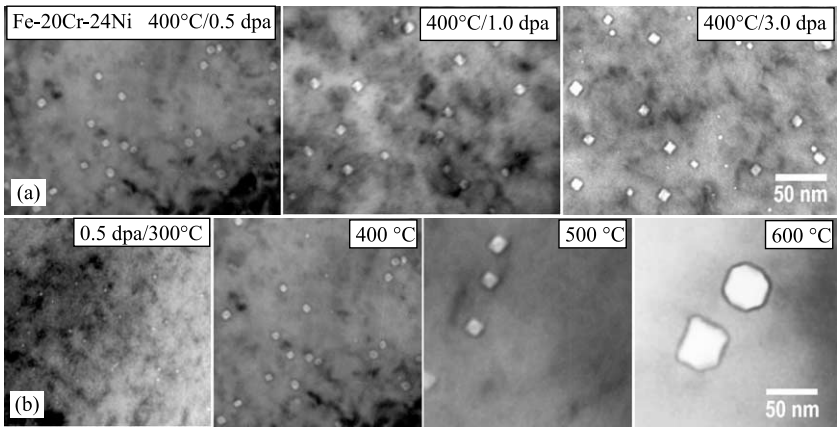

Fig. 8. Photomicrographs showing voids in proton-irradiated high purity alloy Fe–20Cr–24Ni (a) as a function of dose at 400°C and (b) as a function of temperature at a dose of 0.5 dpa.

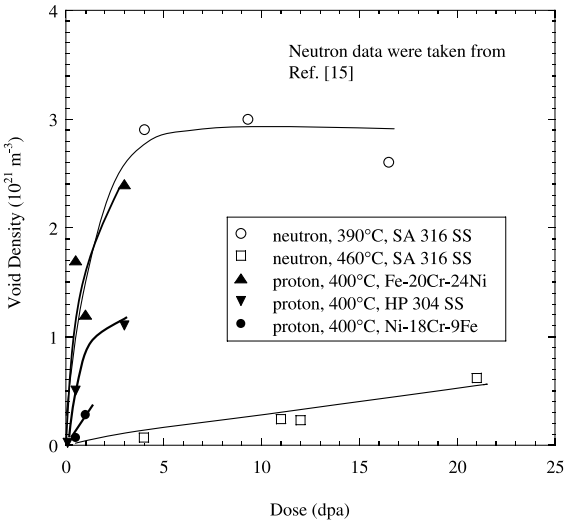

Fig. 9. Dose dependence of void density between neutron-irradiated (390–460°C) austenitic stainless steels [15] and proton-irradiated (400°C) high purity alloys.

lack of data at comparable doses makes the comparison of dose dependence of void density between neutron and proton-irradiations very difficult. Nevertheless, the trends for neutron and proton-irradiation appear similar; a rapid increase at low dose and approach to saturation at higher dose. Void density in Ni–18Cr–9Fe is significantly lower than in Fe–20Cr–24Ni and HP 304 SS. This is consistent with neutron data where swelling was suppressed with higher nickel content (30–75 wt%Ni) [19]. Higher nickel content in austenitic stainless steels delays void development by increasing the vacancy diffusivity [20], changing the void bias induced by radiation-induced segregation [21] and altering the dislocation bias [22,23].

Voids were not observed in proton-irradiated commercial purity CP 304 and CP 316 SS up to doses of 5.0 dpa. The difference in proton-irradiated high purity and commercial purity alloys in void microstructure indicates that the minor constituent has a stronger effect on void swelling than does the major element. The higher silicon content in CP 304 and CP 316 SS (~1.2 at.%) than in high purity alloys (<0.09 at.%) suppresses voids by increasing the vacancy diffusivity and reducing the vacancy supersaturation [18]. The higher phosphorus in commercial alloys (~0.05 at.%) than in high purity alloys (<0.01 at.%) may also play a role by enhancing the loop nucleation, thus increasing the vacancy sink strength. The higher carbon content in solution in commercial alloys (~0.17 at.%) than in high purity alloys (<0.021 at.%) may suppress voids by screening dislocation stress field [24]. The composition effect on void microstructure appeared the same between neutron and proton-irradiation.

In neutron-irradiation, transmutation-produced helium likely plays an important role in void nucleation. For proton-irradiation, no helium is available, and void nucleation is driven by vacancy supersaturation due to the higher production rate of freely migrating defects. Once nucleated, the void microstructure develops in a similar way for neutron and proton-irradiation. It has been proposed that the injection of hydrogen by proton-irradiation might help to nucleate voids [25]. Due to the difficulty in measuring hydrogen in the metal, its role on void formation in austenitic stainless steel cannot be determined. However, the fact that voids can form in thin foils of stainless steel (the 25 μm thickness is less than the proton range) irradiated with 4 MeV protons at 400°C [26] suggests that voids can nucleate and grow without the presence of hydrogen in proton irradiation. Despite potential differences in the mechanism of void nucleation for neutron and proton-irradiation, the dose

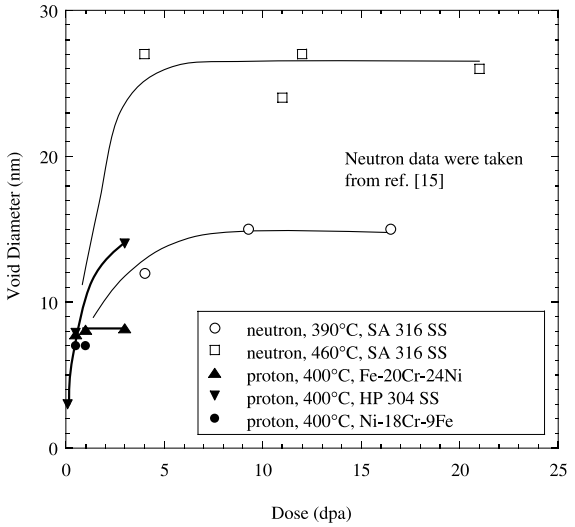

Fig. 10. Dose dependence of void size between neutron-irradiated (390–460°C) austenitic stainless steels [12] and proton-irradiated (400°C) high purity alloys.

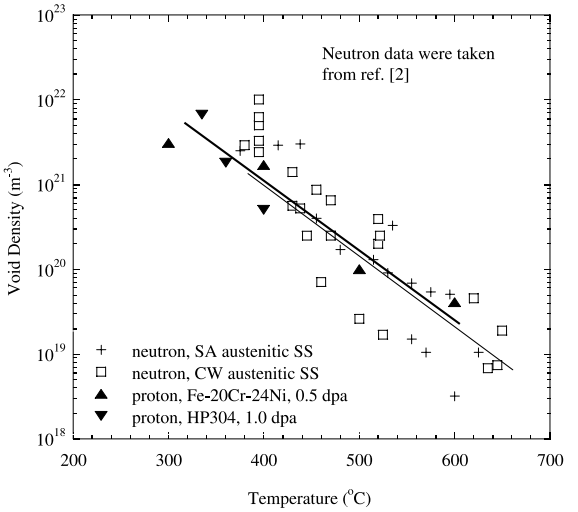

Fig. 11. Temperature dependence of void density for neutron-irradiated austenitic stainless steels [2] and proton-irradiated high purity alloys.

dependence of void density between the two appeared similar.

Void diameter as a function of dose for both neutron and proton irradiation is shown in Fig. 10. The lack of data for both proton irradiation at higher doses and neutron-irradiation at lower doses is problematic. Unfortunately, this was the most relevant comparison which could be made with available data. The rapid saturation in proton-irradiated, high purity alloy Fe–20Cr–24Ni may be caused by the compositional effect, which is consistent with accelerated RIS in high purity Fe–20Cr–9Ni [27]. The difference in the magnitude of void sizes at saturation is obvious. The smaller void size at saturation for proton irradiation may reflect the lack of void coarsening that could have a strong effect on the size.

3.4. Temperature dependence

Photomicrographs of voids as a function of irradiation temperature for high purity alloy Fe–20Cr–24Ni are shown in Fig. 8(b). The temperature dependence of void density for neutron-irradiated austenitic stainless steels and proton-irradiated high purity Fe–20Cr–24Ni is shown in Fig. 11. The trends between neutron and proton-irradiation are similar. Proton data fall well within the neutron data-band except at 300°C where no voids were found in neutron-irradiation. The presence of voids in proton-irradiated high purity alloys at temperature as low as 300°C indicates that proton irradiation is more effective in promoting vacancy supersaturation through the higher point defect production rate than is neutron irradiation. For neutron-irradiation at 300°C, the high sink densities associated with the thermally stable 'black-spot' defect clusters created in the displacement cascade suppress the vacancy supersaturation and inhibit void nucleation and growth. The agreement between proton and neutron-irradiation data at temperatures of 390°C or higher suggests that, despite the fundamental difference in void nucleation, the growth of voids is equivalent. The lack of void nucleation via the helium mechanism is balanced by the enhanced production of freely migrating vacancies in proton-irradiation due to the higher damage rate and displacement efficiency [28].

Void diameter as a function of temperature for high purity alloys irradiated with protons to 0.5–3.0 dpa, and SA 316 SS irradiated with neutrons to 15–25 dpa is shown in Fig. 12. The trends for the proton-irradiated high purity alloys are in agreement with neutron data. The magnitude of void diameter in proton-irradiated Fe–20Cr–24Ni is lower than neutron-irradiated SA 316 SS (15–25 dpa), possibly caused by the lower dose (0.5 dpa) in the case of protons. The temperature dependence of the void diameter for both neutron and proton-irradiations is similar to the loop diameter shown in Fig. 7, indicating that the development of loops and voids are closely correlated.

4. Irradiation-induced hardening

4.1. Dose dependence

The dose dependence of irradiation hardening in proton-irradiated austenitic alloys is shown in Fig. 13(a)

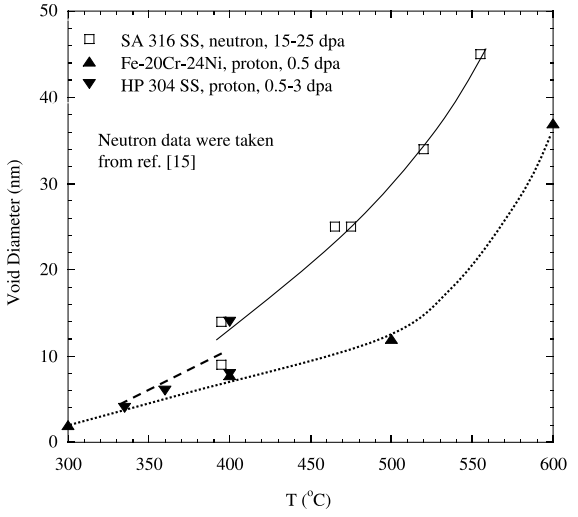

Fig. 12. Temperature dependence of void diameter for SA 316 SS neutron-irradiated to doses of 15–25 dpa [15] and proton-irradiated high purity alloys.

and the comparison of $\Delta\sigma_y$ calculated between DBH model and microhardness measurement is shown in Fig. 13(b). The results calculated from hardness measurement show some difference among the alloys. The high purity alloy showed higher irradiation hardening than commercial alloys at lower dose, despite the higher loop density in the commercial purity alloys. The irradiation hardening in CP 316 SS appeared to continue increasing even up to 5 dpa without slowing down, although starting at the lowest hardening rate (yield strength change per dpa). The reason for the continuous increase in yield strength up to 5 dpa may be caused by a delay in loop saturation in CP 316 SS.

At doses above 1.0 dpa (or yield strength changes above 200 MPa), the yield strength change estimated from Vickers hardness measurement is higher than that estimated from DBH model, Fig. 13(b). The difference increases with dose up to about 300 MPa at 5 dpa and could be due to the fine defect clusters (size <2 nm) that cannot be identified in the microscope. These fine defect clusters could be interstitial clusters or vacancy clusters. It is possible that the tiny defect clusters which were not characterized might play an important role in irradiation hardening. Assuming that these fine defects (such as black-dots) are faulted loops with diameters of <2 nm and barrier strength $\alpha = 0.2$ [29], the difference of 100 MPa corresponds to a loop density of 2×10^{22} m^{-3} which is well within the range of measurements of black dot density [2]. If this is indeed the case, it is expected that the hardening determined from Vickers hardness measurements should be higher than that determined from microstructure measurement

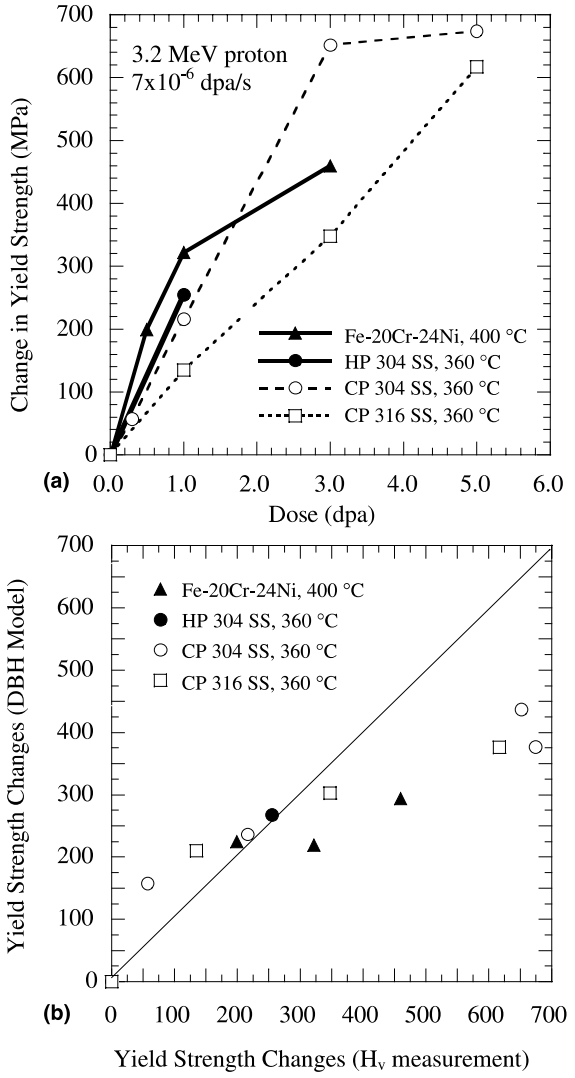

Fig. 13. Dose dependence of yield strength change (a) evaluated from microhardness measurements and (b) the comparison of the $\Delta\sigma_y$ calculated from DBH model with that from microhardness measurements for austenitic alloys irradiated with protons at 360°C and 400°C.

calculated using Eq. (3) for both proton and neutron-irradiation [30].

The comparison of irradiation hardening between proton and neutron results is shown in Fig. 14. The neutron data for 300-series austenitic alloys irradiated and tested at around 300°C [16,31,32] and CP 304 SS and CP 316 SS irradiated at 275°C and tested at room temperature were shown in Fig. 14(a). To increase the clarity for comparison, two lines were drawn to mark the boundaries of the neutron data, Fig. 14(a), then the neutron data were removed except for neutron-irradiated CP 304 SS and CP 316 SS, and proton data

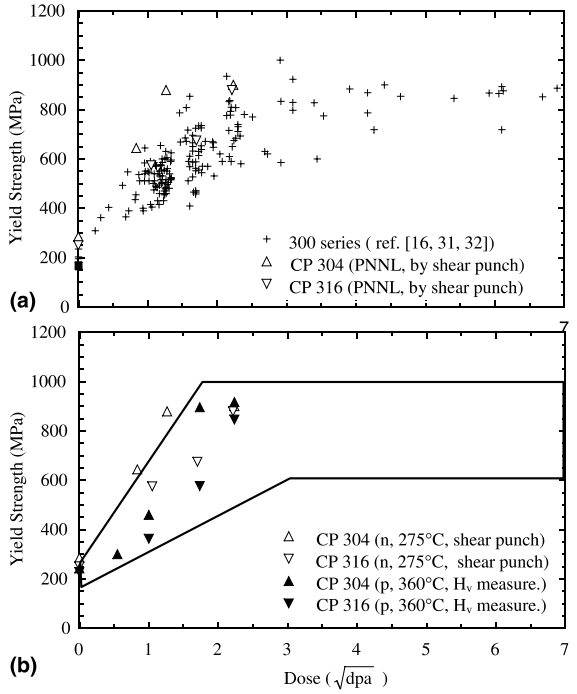

Fig. 14. Measured yield strength of: (a) neutron-irradiated 300-series austenitic alloys (irradiated and tested at about 300°C) [16,31,32] and CP 304 and 316 SS (irradiated at 275°C and tested at RT) [13], (b) yield strength comparison between neutron-irradiated and proton-irradiated CP 304 SS and CP 316 SS (tested at RT) plotted over the neutron data-band for 300-series.

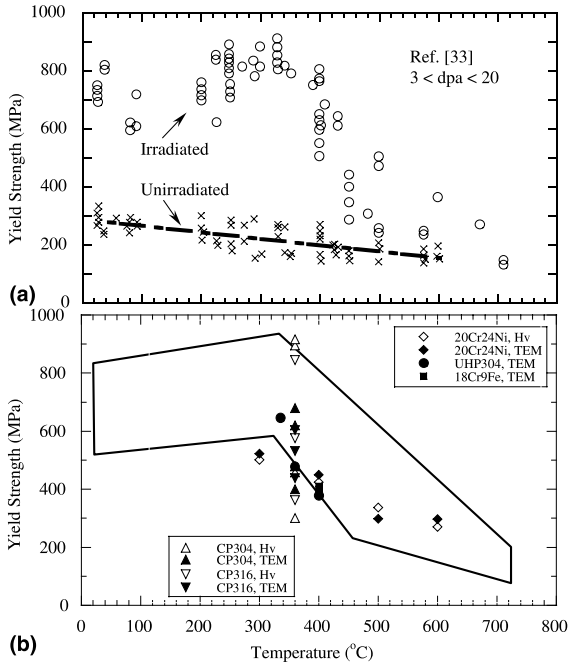

Fig. 15. Temperature dependence of yield strength of: (a) neutron-irradiated (3–20 dpa) 316 SS [33] and (b) its comparison with proton-irradiated (0.5–5.0 dpa) austenitic stainless steels. For proton data, yield strength is estimated from hardness measurements (solid symbols), and from microstructure measurements (open symbols).

were superimposed on the boundaries for comparison, Fig. 14(b). An unirradiated yield strength value of 243 MPa for CP 304 SS and 228 MPa for CP 316 SS was added to the irradiation-induced yield strength change to obtain the irradiated yield strength. The proton data are within the neutron data-band. Note that the mechanical tests for neutron-irradiated CP 304 SS and CP 316 SS (ABB) and proton-irradiated alloys (UM) were conducted at room temperature while the rest of the neutron data were for a test temperature of about 300°C. However, the comparison in Fig. 14(b) is still valid since the changes of yield strength are sensitive to the irradiation temperature, but not to the test temperature, as shown in Fig. 15. The dose dependence of irradiation hardening between neutron- and proton-irradiated same heats of CP 304 SS and CP 316 SS is in reasonable agreement. That the proton data fall within the neutron data-band is expected since the irradiation condition was designed to generated equivalent microstructure for LWR conditions around 300°C. The close agreement with neutron data justified the use of proton-irradiation to produce the same amount of irradiation hardening as does neutron-irradiation.

4.1.1. Temperature dependence

The temperature dependence of irradiation hardening for proton-irradiated austenitic alloys (0.5–5.0 dpa) and neutron-irradiated 316 SS (3–20 dpa) [33] is shown in Fig. 15. The large variation at a given temperature for neutron data are due to the difference in dose and material condition (CW level, heat treatment and composition, etc.). To increase the clarity, the data are bounded and the proton data are plotted over the bounded area, Fig. 15(b). Yield strength as a function of temperature for proton-irradiated austenitic alloys fall within the neutron data-band. The fact that proton data fall on the lower side of the neutron data-band is expected because the doses for the proton irradiation (0.5–5.0 dpa) are lower than that for neutron-irradiation data (3–20 dpa). Considering the difference in test temperature for yield strength between neutron and proton data, yield strength as a function of test temperature for unirradiated 316 SS in Fig. 15(a) can be used to estimate the room-temperature yield strength for the alloys neutron-irradiated at different temperatures. Due to the slow changes of yield strength with test temperature, the effect of difference in test temperatures between neutron and proton data on yield strength comparison in Fig. 15(b) is small. The trends in both proton and neutron-

Table 4
Summary of microstructure and microhardness data with the calculated yield strength changes for both high purity and commercial alloys irradiated with proton at various temperatures and doses[a]

Irradiated temperature (°C)	Irradiated dose (dpa)	Loop density 10^{21} m^{-3}	Loop size (nm)	Percent faulted (%)	Faulted loop density 10^{21} m^{-3}	Void Density 10^{21} m^{-3}	Void size (nm)	Void volume (nm^3)	Swelling (%)	Vickers H_V (kg/mm^2)	Calculated $\Delta\sigma_y^{Hv}$ (MPa)	Calculated $\Delta\sigma_y^{TEM}$ (MPa)
Ni–18Cr–9Fe												
400	0.1	1.9	18	90	1.7	None	None	None	None	NM	NM	129
400	0.3	2.6	13	90[b]	2.3	None	None	None	None	NM	NM	128
400	0.5	3.7	18	90	3.3	0.07	7	NM	NM	NM	NM	185
400	1.0	2.1	24	90[b]	1.9	0.28	7	206	0.0058	NM	NM	175
Fe–20Cr–24Ni												
300	0.5	32	8	50[b]	16	3.1	2	6.6	0.0020	214	277	298
400	0.5	1.3	16	50	0.65	1.7	7.8	276	0.049	192	199	225
400	1.0	3.6	16	50[b]	1.8	1.2	8.1	399	0.050	227	322	219
400	3.0	4.7	16	50	2.4	2.4	8.2	486	0.13	266	460	294
500	0.5	0.092	49	50[b]	0.046	0.10	12	1587	0.016	168	113	73
600	0.5	None	None	50[b]	None	0.041	37	7337	0.031	149	46	72
Fe–20Cr–9Ni (HP 304 SS)												
335	1.0	26	8	80[b]	21	6.7	4	37	0.025	NM	NM	422
360	1.0	5.5	12	80[b]	4.4	1.8	6	178	0.033	248	255	254
400	0.1	0.5	13	80[b]	0.4	0.02	3	NM	NM	NM	NM	56
400	0.5	1.5	16	80	1.2	0.5	7.9	242	0.012	NM	NM	154
400	3.0	2.0	23	80[b]	1.6	1.1	14	1507	0.19	NM	NM	268
CP 304SS												
360	0.3	NM	5.8	NM[c]	8	None	None	None	None	216	57	158
360	1.0	NM	4.9	NM[c]	21	None	None	None	None	261	216	236
360	1.0	17	8	80[b]	14	None	None	None	None	NM	NM	246
360	3.0	NM	6.2	NM[c]	57	None	None	None	None	384	652	437
360	5.0	NM	5.6	NM[c]	47	None	None	None	None	390	674	377
CP 316SS												
360	1.0	NM	6.8	NM[c]	12	None	None	None	None	228	135	210
360	1.0	14	8	80[b]	11	None	None	None	None	NM	NM	222
360	3.0	NM	6.3	NM[c]	27	None	None	None	None	288	348	303
360	5.0	NM	6.7	NM[c]	39	None	None	None	None	364	617	376

[a] NM: not measured.
[b] Values are assumed.
[c] Densities and diameters are for the faulted loops measured from rel-rod DF photos.

irradiation are similar, irradiation hardening decreases as irradiation temperature increases.

All the proton results discussed are summarized in Table 4. Note that faulted loop density in commercial purity alloys is higher than that in high purity alloys, while the loop size in commercial purity alloys is smaller. Although voids are present in high purity alloys, the amount of swelling is negligible.

5. Summary

The objective of this work was to understand the microstructure evolution of proton-irradiated austenitic stainless steels under irradiation conditions relevant to LWR core components. The following points summarize the results of the study:

(1) The irradiation-induced microstructure in proton-irradiated austenitic stainless steels consists mainly of dislocation loops and voids for high purity alloys and dislocation loops only for commercial purity alloys up to 5.0 dpa.

(2) The dose dependence of the dislocation loop density and size in proton-irradiated Fe–Cr–Ni alloys follows the same trend as in neutron-irradiated alloys. High purity alloys show a rapid increase in loop density at doses below 1.0 dpa. The higher loop density in commercial alloys is probably due to enhanced nucleation of loops by minor constituent elements such as phosphorus and silicon.

(3) The temperature dependence of dislocation loop density and size in proton-irradiated Fe–Cr–Ni alloys follows the same trend as in neutron-irradiated alloys. Loop density and size are strong functions of irradiation temperature with the number density decreasing and size increasing as temperature increases.

(4) The dose and temperature dependence of void density and size in proton-irradiated high purity Fe–Cr–Ni alloys follow the same trends as in neutron-irradiated alloys. The development of voids in Ni–18Cr–9Fe is suppressed by the higher nickel content. The lack of voids in the commercial purity alloys is probably due to the minor elements (silicon, phosphorus and carbon).

(5) Yield strength in proton-irradiated austenitic alloys as a function of dose and temperature are consistent with the neutron data trend. The divergence at higher dose is likely due either to the effect of very small loops or on the limitation of the dispersed-barrier-hardening model.

(6) The difference in the character of the displacement cascade on loop nucleation between neutron-irradiation (275°C, 7×10^{-8} dpa/s) and proton-irradiation (360°C, 7×10^{-6} dpa/s) has little effect on the final irradiated microstructure. The reduced level of loop nucleation by in-cascade interstitial clustering in proton-irradiation appears to be balanced by the higher cascade efficiency, the higher dose-rate and the lower sink strength at the higher irradiation temperature.

Acknowledgements

The authors would like to thank Jeremy Busby, Matt Daniel, Todd Allen, John Cookson and other members in the IASCC group at the University of Michigan for their support through the experiment and discussion. Special thanks to Dr Danny Edwards and Dr Stephen Bruemmer at the Pacific Northwest National Laboratory for their support and contribution to this work. The authors are grateful to Dr Victor Roterbug for his help on the proton-irradiation at the Michigan Ion Beam Laboratory. This work was supported by the EPRI under contract number WO4068-26, US Department of Energy under grant DE-FG02-93ER-12310 at the University of Michiganand the Material Science Branch of the Office of Basic Energy Science, US Department of Energy, under contract DE-ACO6-76RL0 1830 with Battelle Memorial Institute.

References

[1] P.J. Maziasz, C.J. McHargue, Int. Mater. Rev. 32 (1987) 190.
[2] S.J. Zinkle, P.J. Maziasz, R.E. Stoller, J. Nucl. Mater. 206 (1993) 270.
[3] G.E. Lucas, J. Nucl. Mater. 206 (1993) 287.
[4] J.M. Cookson, R.D. Carter Jr., D.L. Damcott, M. Atzmon, G.S. Was, J. Nucl. Mater. 202 (1993) 104.
[5] J. Gan, T. Allen, G.S. Was, Mater. Res. Soc. Symp. Proc. 439 (1997) 445.
[6] M.F. Ashby, D.R.H. Jones (Eds.), Engineering Materials, Pergamon, Oxford, 1986.
[7] R.E. Reed-Hill, Physical Metallurgy Principles, 2nd Ed., PWS, Boston, 1973.
[8] D. Damcott, J. Cookson, V. Rotberg, G.S. Was, Nucl. Instrum. and Meth. B 99 (1995) 780.
[9] J.F. Ziegler, J.P. Biersack, U. Littmark, The Stopping and Range of Ions in Solids, Pergamon, New York, 1996.
[10] J. Gan, PhD dissertation, University of Michigan, 1999.
[11] H.R. Higgy, F.H. Hammad, J. Nucl. Mater 55 (1975) 177.
[12] G.E. Taylor, J. Inst. Met. 62 (1938) 307.
[13] S.M. Bruemmer, EPRI report, RP 4068-20, 1997.
[14] Tanaka et al., J. Nucl. Mater. 179 (1991) 572.
[15] Maziasz, ORNL-6121, 1985.
[16] Odette and Lucas, DOE/ER-0313/6, 1989.
[17] K. Fukuya et al., J. Nucl. Mater. 179–191 (1991) 1057.
[18] F.A. Garner, W.G. Wolfer, J. Nucl. Mater. 102 (1981) 143.
[19] F.A. Garner, A.D. Kumar, in: F.A. Garner, N.H. Packan, A.S. Kumar (Eds.), Radiation-Induced Changes in Microstructure: 13th International Symposium (Part I), ASTM STP 955, ASTM, Philadephia, PA, 1987, p. 289.
[20] W.A. Coghlan, F.A. Garner, in: F.A. Garner, N.H. Packan, A.S. Kumar (Eds.), Radiation-Induced Changes

in Microstructure: 13th International Symposium (Part I), ASTM STP 955, ASTM, Philadephia, PA, 1987, p. 315.
[21] F.A. Garner, J. Nucl. Mater. 122&123 (1984) 459.
[22] J.J. Hoyt, F.A. Garner, Fusion Reactor Materials Semi-annual Progress Report DOE/ER-03131/9, US DOE, 1991, p. 81.
[23] T. Muroga, F. Garner, J.M. McCarthy, N. Yoshida, in: R.E. Stoller, A.S. Kumar, D.S. Gelles (Eds.), Effects of Radiation on Materials: 15th International Symposium ASTM STP 1125, ASTM, Philadephia, PA, 1992, p. 1015.
[24] J.F. Bates, R.W. Powell, J. Nucl. Mater 102 (1981) 200.
[25] A. Taylor, S.G. McDonald, Radiation Induced Damage in Metals (1971).
[26] J.A. Hudson, R.S. Nelson, R.J. McElroy, J. Nucl. Mater. 65 (1977) 279.
[27] J.T. Busby, G.S. Was, S.M. Bruemmer, D.J. Edwards, E.A. Kenik, Mater. Res. Soc. Symp. Proc. 540 (1999) 451.
[28] G.W. Was, S.M. Bruemmer, J. Nucl. Mater. 216 (1994) 326.
[29] N. Yoshida, J. Nucl. Mater. 174 (1990) 220.
[30] G.E. Lucas, J. Nucl. Mater. 206 (1993) 287.
[31] M. Kodama et al., in: Proceedings of the 8th International Symposium on Environmental Degradation of Materials in Nuclear Power System Water Reactors, 1998, p. 831.
[32] A. Jensen et al., EPRI report, 1998.
[33] G.E. Lucas, J. Nucl. Mater. 233–237 (1996) 207.